Controllable Emergent Spatial Spin Modulation in Sr$_2$IrO$_4$ by *In Situ* Shear Strain

Shashi Pandey[ORCID],[1] Han Zhang[ORCID],[1,*] Junyi Yang,[1] Andrew F. May,[2] Joshua J. Sanchez,[3,4]
Zhaoyu Liu,[4] Jiun-Haw Chu,[4] Jong-Woo Kim[ORCID],[3] Philip J. Ryan,[3,5] Haidong Zhou,[1] and Jian Liu[ORCID][1,†]

[1]*Department of Physics and Astronomy, University of Tennessee, Knoxville, Tennessee 37996, USA*
[2]*Materials Science and Technology Division, Oak Ridge National Laboratory, Oak Ridge, Tennessee 37831, USA*
[3]*Advanced Photon Source, Argonne National Laboratory, Argonne, Illinois 60439, USA*
[4]*Department of Physics, University of Washington, Seattle, Washington 98195, USA*
[5]*School of Physical Sciences, Dublin City University, Dublin 11, Ireland*

Symmetric anisotropic interaction can be ferromagnetic and antiferromagnetic at the same time but for different crystallographic axes. We show that the competition of anisotropic interactions of orthogonal irreducible representations can be a general route to obtain new exotic magnetic states. We demonstrate it here by observing the emergence of a continuously tunable 12-layer spatial spin modulation when distorting the square-lattice planes in the quasi-two-dimensional antiferromagnetic Sr$_2$IrO$_4$ under *in situ* shear strain. This translation-symmetry-breaking phase is a result of an unusual strain-activated anisotropic interaction which is at the fourth order and competing with the inherent quadratic anisotropic interaction. Such a mechanism of competing anisotropy is distinct from that among the ferromagnetic, antiferromagnetic, and/or the Dzyaloshinskii-Moriya interactions, and it could be widely applicable and highly controllable in low-dimensional magnets.

Exotic spatial spin modulations, including various forms of spin spirals [1,2] and magnetic skyrmions [3–5], have been extensively studied for magnetoelectric effects [6], topology [7,8], spintronics [9–12], etc. Their common origin is competition between ferromagnetic, antiferromagnetic, and/or the Dzyaloshinskii-Moriya (antisymmetric anisotropic) interactions that favor parallel, antiparallel, and orthonormal spin arrangement, respectively. In contrast to these directional interactions, symmetric anisotropic interaction has an axial nature that it could be ferromagnetic for one axial component of the moments and antiferromagnetic for another at the same time. For example, the symmetric part of the two-spin anisotropic exchange tensor derived by Moriya [13] may have a form of $S_i^x S_j^x - S_i^y S_j^y$ or $S_i^x S_j^y + S_i^y S_j^x$, both of which represent symmetric anisotropy but of different irreducible point-group representations. If present at the same time, anisotropies of different symmetry channels would force the moments to different axes, and their competition could be an attractive alternative mechanism for stabilizing exotic magnetic phases. The strategy for realizing such competition could be remarkably simple and general. Since the spontaneous anisotropy often preserves certain rotational or mirror symmetry, one may apply shear strain to break this symmetry to introduce anisotropy of a different irreducible point-group representation.

Sr$_2$IrO$_4$ is one of the most important representatives of magnetic oxides where anisotropic interactions play a key role. Its strong spin-orbit coupling stabilizes an antiferromagnetic (AFM) Mott insulating ground state with the so-called $J_{\rm eff} = 1/2$ moments, which represents the effective angular momentum or pseudospin of the localized electrons [14–28]. Analog to the parent phase of high-T_c cuprates [29–38], Sr$_2$IrO$_4$ exhibits a quasi-2D tetragonal lattice and an AFM ordering below $T_N \sim 230$ K [15,17]. The spontaneous quasi-2D AFM order is stabilized by the interplane symmetric anisotropic interaction and breaks the D_{4h} point-group symmetry with the moments aligned along the a or b axis [Fig. 1(a)], i.e., orthorhombic twin domains of the B_{1g} symmetry [Fig. 1(a)] [39,40]. Introducing anisotropy that favors the $\langle 110 \rangle$ axes, i.e., B_{2g} symmetry, is thus expected to compete with the spontaneous B_{1g} anisotropy. Because of the strong spin-orbit coupling, the pseudospin-half wave function is highly sensitive to the lattice distortion via pseudo-Jahn-Teller effect [40]. Anisotropy of B_{2g} symmetry may be achieved by applying a shear strain to the ab plane [Fig. 1(a)].

Here we report that such anisotropy competition under *in situ* shear strain leads to a surprising translational symmetry-breaking spin modulation along the c axis consisting of 12 IrO$_2$ planes [Fig. 1(a)] that has not been observed before in Sr$_2$IrO$_4$. Our study unambiguously shows that the spatial modulation is a result of competing anisotropy because the shearing turns on a hidden quartic anisotropic interaction of B_{2g} symmetry that is *orthogonal* to the spontaneous quadratic anisotropy of B_{1g} symmetry.
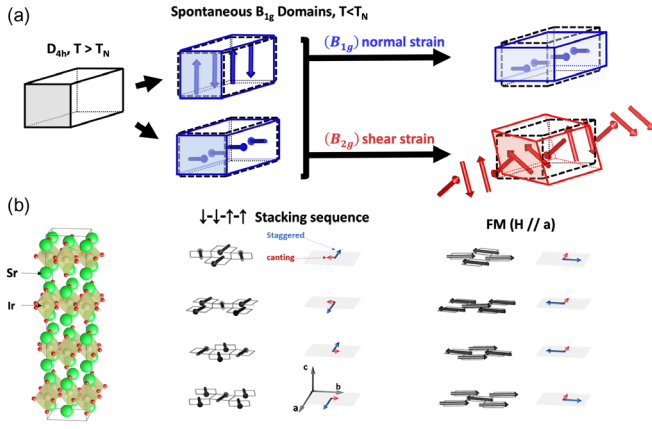
FIG. 1. Schematic of the Sr_2IrO_4 unit cell. (a) Schematic diagram showing symmetry breaking of a tetragonal material by the magnetic order. The blue and red arrows denote the direction of the staggered moments in each IrO_2 plane in a tetragonal cell having four IrO_2 planes. (b) Crystal structure of Sr_2IrO_4, with the $\downarrow$-$\downarrow$-$\uparrow$-$\uparrow$ and FM stacking sequence below $T_N \sim 230$ K. The net moment of each IrO_2 plane (red arrows) is locked with the staggered moment (blue arrows) with fixed chirality and proportionality in each layer.

Moreover, the competition and the modulation can be continuously and efficiently tuned here by applying a strain of less than 0.05%. Our observation of spatially modulated magnetic phases adds a significant representative to the expanding list of emergent phases due to tuning of interactions of different irreducible point-group representations such as electronic nematicity [41,42], quadrupolar order [43,44], and unconventional superconductivity [45–47].

As can be seen in Fig. 1(b), a key feature of Sr_2IrO_4 is the octahedral rotation around the c axis [21], leading to a unit cell expansion from the original Ruddlesden-Popper structure. As a result, the spontaneous AFM order fully preserves the translational symmetry and displays spin canting of the planar Ir AFM moments within the ab plane, which orthogonally locks the net moment and the staggered moment of each IrO_2 plane together with a fixed chirality and ratio [48–50]. Before discussing the shear strain effect, it is important to establish the normal strain effect for comparison. Since the spontaneous orthorhombic distortion is weak [40] and the system can be considered pseudo-tetragonal, applying normal strain, i.e., B_{1g} strain, by external stress has been shown to be highly efficient in detwinning the AFM domains [51,52] [Fig. 1(a)]. A more pronounced effect occurs when the strain is applied with a magnetic field. Since the interplane anisotropic interaction stabilizes a $\downarrow$-$\downarrow$-$\uparrow$-$\uparrow$ (or $\downarrow$-$\uparrow$-$\uparrow$-$\downarrow$) stacking sequence of the IrO_2 planes where $\uparrow$ and $\downarrow$ refer to the net moments [17,39], a sufficiently large field polarizes them through a metamagnetic phase transition [21] to a $\uparrow$-$\uparrow$-$\uparrow$-$\uparrow$ sequence [Fig. 1(b)], which for simplicity we call the
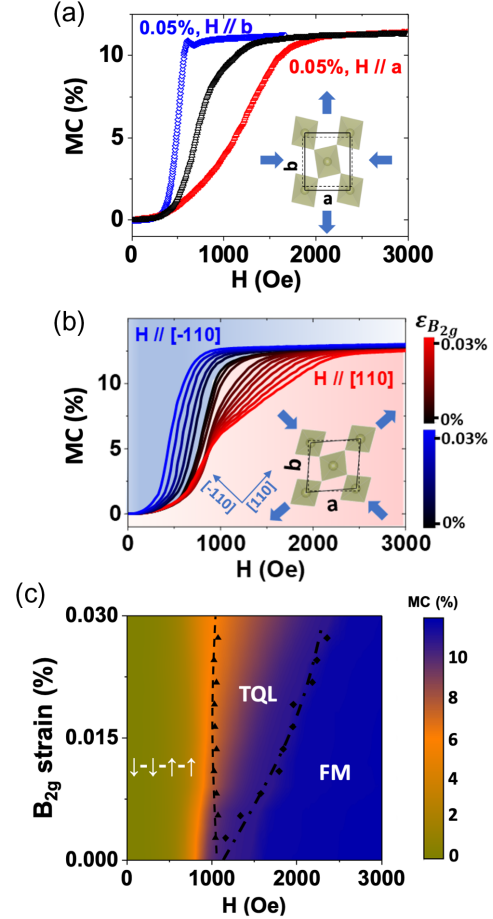

FIG. 2. Magnetoconductance under B_{1g} and B_{2g} strain. (a) MC at 210 K without externally applied strain (black open triangles), under the applied B_{1g} strain with $H\|a$ (red open triangles) and $H\|b$ (blue open squares). (b) MC at 210 K under various B_{2g} strains with $H\|[110]$ and with $H\|[-110]$. Schematic diagrams of the distortions by the B_{1g} and B_{2g} strains are shown in the insets. The distortion is exaggerated for illustration purposes. (c) B_{2g} strain-field phase diagram based on the MC results, where the phase boundaries are extracted from the kink positions in the MC curves. The strain values were calibrated by measuring the lattice parameters with x-ray diffraction (see Supplemental Material [57]).

ferromagnetic (FM) state hereafter. Figure 2(a) shows an example when we applied the field and the $in\ situ$ B_{1g} strain that stretched the a axis and contracted the b axis at 210 K by directly adhering a thin piece of Sr_2IrO_4 single crystal to a piezoactuator, which delivers up to $\sim$0.05% of anisotropic strain [51]. As can be seen, the transition monitored by magnetoconductance (MC) [53–56] is radically sharpened and shifted to a much lower field with $H\|b$, whereas it is significantly broadened and shifted to much higher field with $H\|a$. Such a strong anisotropic response with high tunability is a result of the uniaxial anisotropy induced by the B_{1g} strain that restricts the metamagnetic transition to a

sharp spin-flip or a broad continuous rotation depending on whether the field is parallel or perpendicular to the enforced easy axis [51,52].

The situation becomes much different under the shearing B_{2g} strain [Fig. 2(b)], which stretches the [110] axis and contracts the [−110] axis, i.e., $\varepsilon_{B_{2g}} \equiv (d_{110} - d_{-110})/(d_{110} + d_{-110})$, where d_{110} and d_{-110} represent the d spacing of the (110) and (−110) planes, respectively. The values of d_{110} and d_{-110} were calibrated by measuring the structural peaks with x-ray diffraction [51,57], with a typical standard error of the calculated strain values to be ∼0.004%. As shown in Fig. 2(b), while the transition with $H\|[-110]$ is also sharpened and shifted to lower field at 210 K similar to the case of $H\|b$ under B_{1g} strain, the transition with $H\|[110]$ is clearly broken into two sections by an emerging kink at ∼800 Oe. The section below the kink shows weak strain dependence, whereas the section above is significantly extended to a higher field by increasing $\varepsilon_{B_{2g}}$, giving rise to a prolonged "tail" of an overall "tied-up" shape of the MC curves. An analysis of the derivative of the MC curve [57] reveals a fine movement of the kink that it is slightly up-shifted first before being slightly down-shifted with increasing $\varepsilon_{B_{2g}}$. A B_{2g} strain-field phase diagram can now be constructed from the MC results as shown in Fig. 2(c). A new phase is clearly emerging between the ↓-↓-↑-↑ state and the FM state with phase boundaries defined by the kink and the end point of the tail. This complex behavior is in sharp contrast with the case of $H\|a$ under B_{1g} strain, suggesting a mechanism distinct from uniaxial anisotropy.

To resolve the underlying magnetic structure of the transition under B_{2g} strain, we measured resonant x-ray magnetic scattering of the $(10L)$ and $(-10L)$ magnetic peaks at the Ir L_3 edge under *in situ* B_{2g} strain with $H\|[-110]$ and $H\|[110]$, respectively. With $\varepsilon_{B_{2g}} = 0.015\%$ at 210 K and zero field, we observed the magnetic reflections at $L = 20$ and 22 associated with the two spontaneous B_{1g} twin domains of the ↓-↓-↑-↑ state, respectively [51]. The presence of both domains without detwinning is consistent with the B_{2g} symmetry of the applied strain. As shown in Fig. 3(a), when $H\|[-110]$ is turned on to induce the metamagnetic transition, the $L = 21$ peak associated with the FM order parameter of the net moments emerges and increases rapidly at the expense of the $L = 20$ and 22 peaks until both of them vanish. (The $L = 20$ peak vanishes a bit earlier than the $L = 22$ peak due to a small misalignment of the field that suppresses one domain slightly faster than the other.) The overall conversion between the ↓-↓-↑-↑ state and the FM state under B_{2g} strain when the field is parallel to the contracted axis is similar to that in the strain-free sample [58]. The only difference is the down-shifting of the critical field to the region of ∼500–700 Oe, consistent with the MC data.
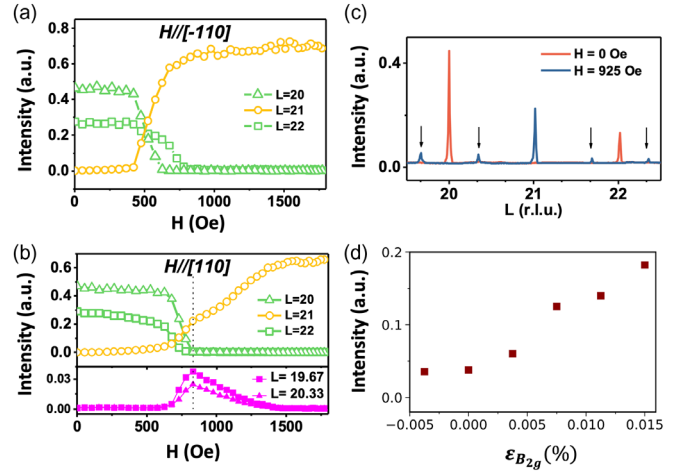
FIG. 3. Resonant x-ray magnetic scattering. (a) Evolution of the (1 0 20-22) magnetic reflections associated with the two twin domains of the ↓-↓-↑-↑ state and the FM state as functions of the external magnetic field when $H\|[-110]$ and $\varepsilon_{B_{2g}} = 0.015\%$. (b) Evolution of the equivalent (−1 0 20-22) magnetic reflections when $H\|[110]$ and $\varepsilon_{B_{2g}} = 0.015\%$ is shown on the top panel. The bottom panel shows the evolution of $(-1\,0\,19\frac{2}{3})$ and $(-1\,0\,20\frac{1}{3})$ peaks. (c) L scans of the $(-10L)$ rod when $H\|[110]$ and $\varepsilon_{B_{2g}} = 0.015\%$. The blue curve taken at $H = 925$ Oe shows the emergence of 1/3 satellite peaks highlighted by the black arrows. The red curve taken at zero field is shown for comparison. (d) The emergence and increase of the $(-1\,0\,19\frac{2}{3})$ peak intensity as a function of the varying strain from −0.004% to 0.015%.

The transition process turns out very differently with $H\|[110]$ as shown in Fig. 3(b). When both $L = 20$ and 22 peaks drop to zero at 825 Oe, the $L = 21$ peak only gains a partial increase that is far from its saturated value. Most of the intensity is instead from a slow increase from 825 to 1500 Oe. The slope change at 825 Oe leads to a clear kink and an overall shape that highly resembles the MC curve, suggesting that the extended region above the kink is neither the ↓-↓-↑-↑ state nor the FM state but a distinct new state with a finite FM component. After performing a survey at other L positions at 925 Oe such as that shown in Fig. 3(c), we discovered emerging satellite magnetic peaks at $L = 2n \pm 1/3$, indicating translational symmetry breaking along the c axis with a tripled size. Such a 12-IrO$_2$-plane modulation of the staggered moment corresponds to a 6-IrO$_2$-plane modulation of the net moment according to the out-of-phase octahedral rotation within the structural cell [Fig. 1(b)]. We denote this state as the triquadrupole-layer (TQL) state hereafter to represent the spin modulation containing three four-layer unit cells. The field dependence of the satellite peak intensities displayed in Fig. 3(b) exhibits a clear correlation with the integer peaks. It is now apparent that the ↓-↓-↑-↑ state first transforms into the TQL state, and the FM component of the TQL state gradually increases at the expense of the amplitude of the spatial modulation until reaching the FM state. Figure 3(d)

further shows the increase of the satellite peak intensity at 925 Oe as a function of $\varepsilon_{B_{2g}}$, demonstrating that the B_{2g} strain not only stabilizes the spatial modulation but is also able to tune its amplitude. These results confirm the new phase in the phase diagram [Fig. 2(c)] to be the TQL state.

The emergence of the TQL state corroborates that the B_{2g} strain effect is to compete with the spontaneous anisotropy that favors B_{1g} symmetry rather than changing the easy axis. To unveil this competition, we investigated the minimal free-energy model that captures the TQL state. Because of the robust intraplane AFM order and the locking between the net moment and staggered moment [49], the stacking of the quasi-2D planes can be modeled as an effective 1D system of the net moments $M_j = MS_j$, where M is the moment size and S_j is the unit vector in the ab plane characterized by angle θ_j with respect to the a axis. The ↓-↓- ↑ - ↑ state, TQL state, and FM state are thus characterized by a 1D wave vector $q = 1/4$, $1/6$, and 0, respectively. The free energy can be written as

$$F(M_j) = E_0 + E_H + E_{B_{1g}} + E_{B_{2g}}, \qquad (1)$$

where E_0 includes inherent interactions that account for the spontaneous ↓-↓- ↑ - ↑ state of B_{1g} symmetry, E_H is the Zeeman energy, and $E_{B_{1g}}$ and $E_{B_{2g}}$ represent interactions induced by the externally applied strain of B_{1g} and B_{2g} symmetry, respectively. At a fixed temperature below T_N, M is considered as a constant under the perturbations of field and strain, and it is $\sim 0.04 \mu_B$ at 210 K according to magnetization. Thus, all θ_j-independent terms are neglected, and the ground state is obtained by energy minimization with respect to θ_j. By mapping the reported interplane anisotropic interactions and the pseudospin-lattice coupling of Sr_2IrO_4 [40,51] to this effective model, one has

$$E_0 = \delta_c \sum_j (-1)^j (S_j^a S_{j+1}^a - S_j^b S_{j+1}^b) - k_b \sum_j Q_j^{(1)2}$$
$$- k_b' \sum_j Q_j^{(1)} Q_{j+1}^{(1)}, \qquad (2)$$

where $Q_j^{(1)} \equiv S_j^{a2} - S_j^{b2}$ is the quadrupole of B_{1g} symmetry. The δ_c term is the anisotropic exchange interaction of B_{1g} symmetry with an alternating sign that favors a $q = 1/4$ modulation. It becomes the ↓-↓- ↑ - ↑ state with the k_b term and the k_b' term, which have the A_{1g} symmetry and force the moments along the a or b axis [39,40] (see Supplemental Material [57]). We constrain δ_c, k_b, and k_b' by reproducing the metamagnetic transition at zero strain and under the B_{1g} strain by including a uniaxial anisotropy term in $E_{B_{1g}}$ [51] (Fig. S3 of Ref. [57]).

Next we turn off $E_{B_{1g}}$ and proceed to simulate the B_{2g} strain effect. We first tried B_{2g} symmetry terms of uniaxial and exchange anisotropy. But both fail to describe the [57].
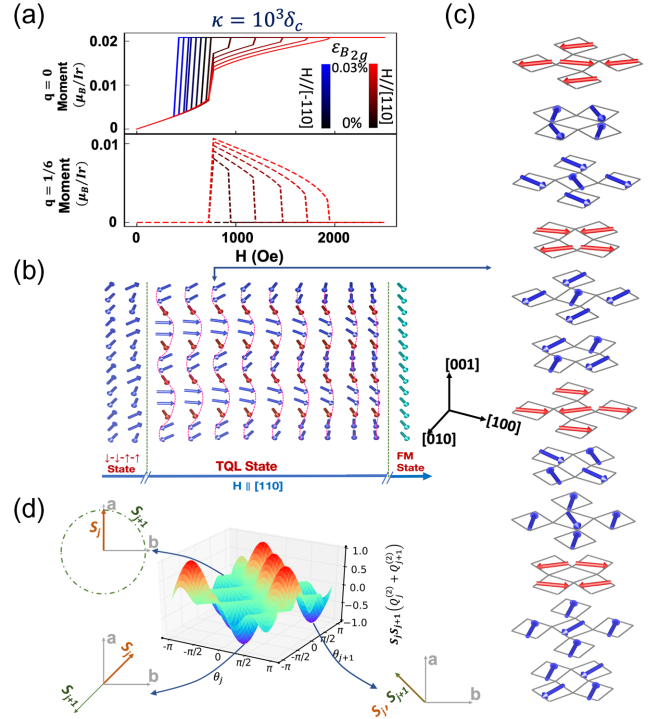

FIG. 4. Simulation of the free-energy model. (a) Simulation of metamagnetic transition when including the κ term that is coupled to B_{2g} strain. The solid lines represent the order parameter of the $q = 0$ (FM) state while the dashed line is for the $q = 1/6$ (TQL) state. The coupling coefficient $\kappa = 10^3 \delta_c$. (b) Schematic diagram showing the net moment evolution during the ↓↓ ↑↑-TQL-FM metamagnetic phase transition. The full magnetic structure in a 12-IrO_2-layer cell is shown in (c) for one of the TQL configurations. (d) 3D contour plot of the energy of the κ term. The insets demonstrate the configuration of two neighboring net moments at the minima and saddle points.

This inconsistency leads us to consider increasing the order of the anisotropic interaction from quadratic to quartic. The only nontrivial quartic term of B_{2g} symmetry has the form [57]

$$E_{B_{2g}} = \varepsilon_{B_{2g}} \kappa \sum_j S_j \cdot S_{j+1} (Q_j^{(2)} + Q_{j+1}^{(2)}), \qquad (3)$$

or equivalently,

$$E_{B_{2g}} = \varepsilon_{B_{2g}} \kappa \sum_j S_j \cdot (S_{j-1} + S_{j+1}) Q_j^{(2)}, \qquad (4)$$

where $Q_j^{(2)} \equiv S_j^a S_j^b$ is the quadrupole of B_{2g} symmetry and κ is the coupling coefficient. Figure 4(a) shows the calculated metamagnetic transition, which is characterized by the $q = 0$ order parameter and turns out to capture the observed characteristics remarkably well, especially the two-section shape of the transition with an extended tail region when $H\|[110]$. Even the fine movement of the kink

in the MC curve is mimicked by the strain dependence of the critical field that separates the two sections. More importantly, this quartic anisotropy correctly predicts a finite $q = 1/6$ modulation within the tail region where the $q = 1/6$ modulation appears and slowly decreases with increasing field.

Figure 4(b) shows a representative evolution of the simulated spatial modulation. Initially, the moments cant away from the a/b axis toward [110] to gain Zeeman energy while staying in pairs to maintain the ↓-↓-↑-↑ state. When the field increases further, the $q = 1/6$ modulation sets in by "inserting" an unpaired site in between the adjacent pairs and breaking the translation symmetry. The modulation amplitude of this TQL state then slowly decreases with increasing field until both the unpaired and paired moments become fully aligned. The periodic emergence of the unpaired sites is evidently the key since it plays a domain wall-like role in separating the pairs, allowing the κ term to save more energies on the paired sites while letting the δ_c interaction to concentrate more on the unpaired site. The full 12-IrO$_2$-layer magnetic structure is also shown for one of the TQL configurations as an example to illustrate the modulation in Fig. 4(c).

Given the excellent agreement with the experiment, we comment on the important differences of the quartic anisotropic interaction from the usual quadratic ones, and why it enables the emergent TQL state. Specifically, while it is similar to quadratic anisotropic interactions [Fig. S7(a) in Supplemental Material [57]] in that the two moments couple antiferromagnetically and ferromagnetically along the two principle axes, respectively [Fig. 4(d)], increasing the order of anisotropic interaction necessarily allows more intermediate angular configurations with no energy gain or loss, i.e., nodes or saddle points in the energy landscape [the green regions in Fig. 4(d)]. This can be understood from Eq. (4), where the nearest-neighbor interaction is *gated* by $Q_j^{(2)}$, controlling the sign of the interaction to be positive or negative. If this term is dominant, the stacking sequence of the canted moments would be either ferromagnetic along [1−10] or antiferromagnetic along [110] [Fig. S7(b) [57]]. However, neither of these two states is spatially modulated, although both are clearly different from the spontaneous ↓-↓-↑-↑ sequence with moments along [100] or [010]. What is more important is that, whenever S_j is along the a/b axis, i.e., $Q_j^{(2)} = 0$, the quartic interaction would be zero regardless of the direction of S_{j-1} and S_{j+1}. This character is absent in quadratic interactions [Fig. S7(a) [57]] and provides more options to find compromised configurations when competing with the δ_c interactions of orthogonal symmetry. Thus, to stabilize the modulation, the anisotropy competition is necessary. We further confirmed this by simulating a hypothetical situation where the A_{1g}, k_b and k_b' terms are removed [Fig. S8 [57]).

The presence of $Q_j^{(2)}$ can be understood from the pseudospin-lattice coupling between the octahedral distortion and the $J_{\text{eff}} = 1/2$ wave function [14,40]. A distortion of B_{2g} symmetry would mediate the relative weight between the xz and yz orbitals and enables B_{2g} pseudospin quadrupole formed by two neighboring sites within the same layer. In contrast, a distortion of B_{1g} symmetry would mediate the relative weight between the az and bz orbitals and enables B_{1g} pseudospin quadrupole.

Overall, we demonstrate that introducing anisotropy that is orthogonal to the spontaneous anisotropy could lead to translational symmetry breaking and spatial spin modulation. The possibility of introducing the competition between the B_{1g} and B_{2g} anisotropy in Sr$_2$IrO$_4$ by *in situ* shear strain allows continuous tuning of the spatial modulation. This approach to trigger competition and obtain controllable new phases could be applicable to many quasi-2D materials, where the anisotropy plays a vital role in stabilizing the ordering and the magnetoelastic coupling is efficient for strain-induced anisotropy. The emergence of the B_{2g} quartic interaction also highlights the rich unexplored physics of higher-order anisotropy. To our knowledge, quartic anisotropic interaction has not been observed before. Since quartic exchange interactions in Mott insulators arise from the fourth-order perturbation [59], the multiple hopping processes must involve both interorbital and intraorbital hopping at the same time. The anisotropy represented by the quadrupole is likely due to interorbital hopping within the IrO$_2$ plane, while the interplane coupling component is isotropic and likely driven by intraorbital hopping. These results should motivate theoretical investigations on extracting the underlying microscopic model as well as exploration of high-order anisotropic interactions in other materials.

———————————

[*]Corresponding author.
hanzhang@cczu.edu.cn
[†]Corresponding author.
jianliu@utk.edu

[1] S.-W. Cheong and M. Mostovoy, Multiferroics: A magnetic twist for ferroelectricity, Nat. Mater. **6**, 13 (2007).

[2] J. Herbrych, J. Heverhagen, G. Alvarez, M. Daghofer, A. Moreo, and E. Dagotto, Block-spiral magnetism: An exotic type of frustrated order, Proc. Natl. Acad. Sci. U.S.A. **117**, 16226 (2020).

[3] W. Jiang, G. Chen, K. Liu, J. Zang, S. G. E. te Velthuis, and A. Hoffmann, Skyrmions in magnetic multilayers, Phys. Rep. **704**, 1 (2017).

[4] N. Nagaosa and Y. Tokura, Topological properties and dynamics of magnetic skyrmions, Nat. Nanotechnol. **8**, 899 (2013).

[5] Y. Zhou, Magnetic skyrmions: Intriguing physics and new spintronic device concepts, Natl. Sci. Rev. **6**, 210 (2019).

[6] M. Fiebig, Revival of the magnetoelectric effect, J. Phys. D **38**, R123 (2005).

[7] M. Sato and Y. Ando, Topological superconductors: A review, Rep. Prog. Phys. **80**, 076501 (2017).

[8] S. Rachel, Interacting topological insulators: A review, Rep. Prog. Phys. **81**, 116501 (2018).

[9] V. Baltz, A. Manchon, M. Tsoi, T. Moriyama, T. Ono, and T. Tserkovnyak, Antiferromagnetic spintronics, Rev. Mod. Phys. **90**, 015005 (2018).

[10] T. Jungwirth, X. Marti, P. Wadley, and J. Wunderlich, Antiferromagnetic spintronics, Nat. Nanotechnol. **11**, 231 (2016).

[11] P. Němec, M. Fiebig, T. Kampfrath, and A. V. Kimel, Antiferromagnetic opto-spintronics, Nat. Phys. **14**, 229 (2018).

[12] L. Šmejkal, Y. Mokrousov, B. Yan, and A. H. MacDonald, Topological antiferromagnetic spintronics, Nat. Phys. **14**, 242 (2018).

[13] T. Moriya, Anisotropic superexchange interaction and weak ferromagnetism, Phys. Rev. **120**, 91 (1960).

[14] G. Jackeli and G. Khaliullin, Mott Insulators in the Strong Spin-Orbit Coupling Limit: From Heisenberg to a Quantum Compass and Kitaev Models, Phys. Rev. Lett. **102**, 017205 (2009).

[15] G. Cao, J. Bolivar, S. McCall, and J. E. Crow, Weak ferromagnetism, metal-to-nonmetal transition, and negative differential resistivity in single-crystal Sr_2IrO_4, Phys. Rev. B **57**, R11039 (1998).

[16] B. J. Kim et al., Novel $J_{eff} = 1/2$ Mott State Induced by Relativistic Spin-Orbit Coupling in Sr_2IrO_4, Phys. Rev. Lett. **101**, 076402 (2008).

[17] B. J. Kim, H. Ohsumi, T. Komesu, S. Sakai, T. Morita, H. Takagi, and T. Arima, Phase-sensitive observation of a spin-orbital Mott state in Sr_2IrO_4, Science **323**, 1329 (2009).

[18] R. Arita, J. Kunes, A. V. Kozhevnikov, A. G. Eguiluz, and M. Imada, Ab Initio Studies on the Interplay Between Spin-Orbit Interaction and Coulomb Correlation in Sr_2IrO_4 and Ba_2IrO_4, Phys. Rev. Lett. **108**, 086403 (2012).

[19] W. Witczak-Krempa, G. Chen, Y. B. Kim, and L. Balents, Correlated quantum phenomena in the strong spin-orbit regime, Annu. Rev. Condens. Matter Phys. **5**, 57 (2014).

[20] R. Schaffer, E. Kin-Ho Lee, B. J. Yang, and Y. B. Kim, Recent progress on correlated electron systems with strong spin-orbit coupling, Rep. Prog. Phys. **79**, 094504 (2016).

[21] G. Cao and P. Schlottmann, The challenge of spin-orbit-tuned ground states in iridates: A key issues review, Rep. Prog. Phys. **81**, 042502 (2018).

[22] J. Bertinshaw, Y. K. Kim, G. Khaliullin, and B. J. Kim, Square Lattice Iridates, Annu. Rev. Condens. Matter Phys. **10**, 315 (2019).

[23] S. Boseggia, R. Springell, H. C. Walker, H. M. Rønnow, Ch. Rüegg, H. Okabe, M. Isobe, R. S. Perry, S. P. Collins, and D. F. McMorrow, Robustness of Basal-Plane Antiferromagnetic Order and the J(eff) = 1/2 State in Single-Layer Iridate Spin-Orbit Mott Insulators, Phys. Rev. Lett. **110**, 117207 (2013).

[24] D. H. Torchinsky, H. Chu, L. Zhao, N. B. Perkins, Y. Sizyuk, T. Qi, G. Cao, and D. Hsieh, Structural Distortion-Induced Magnetoelastic Locking in Sr_2IrO_4 Revealed Through Nonlinear Optical Harmonic Generation, Phys. Rev. Lett. **114**, 096404 (2015).

[25] T. Takayama, A. Matsumoto, G. Jackeli, and H. Takagi, Model analysis of magnetic susceptibility of Sr_2IrO_4: A two-dimensional $J_{eff} = 1/2$ Heisenberg system with competing interlayer couplings, Phys. Rev. B **94**, 224420 (2016).

[26] S. J. Moon, H. Jin, K. W. Kim, W. S. Choi, Y. S. Lee, J. Yu, G. Cao, A. Sumi, H. Funakubo, C. Bernhard, and T. W. Noh, Dimensionality-Controlled Insulator-Metal Transition and Correlated Metallic State in 5d Transition Metal Oxides $Sr_{n+1}Ir_nO_{3n+1}$ (n = 1, 2, and Infinity), Phys. Rev. Lett. **101**, 226402 (2008).

[27] E. Paris et al., Strain engineering of the charge and spin-orbital interactions in Sr_2IrO_4, Proc. Natl. Acad. Sci. U.S.A. **117**, 24764 (2020).

[28] H. Watanabe, T. Shirakawa, and S. Yunoki. Microscopic Study of a Spin-Orbit-Induced Mott Insulator in Ir Oxides, Phys. Rev. Lett. **105**, 216410 (2010).

[29] J. Kim, D. Casa, M. H. Upton, T. Gog, Y.-J. Kim, J. F. Mitchell, M. van Veenendaal, M. Daghofer, J. van den Brink, G. Khaliullin, and B. J. Kim, Magnetic Excitation Spectra of Sr_2IrO_4 Probed by Resonant Inelastic X-Ray Scattering: Establishing Links to Cuprate Superconductors, Phys. Rev. Lett. **108**, 177003 (2012).

[30] Y. K. Kim, O. Krupin, J. D. Denlinger, A. Bostwick, E. Rotenberg, Q. Zhao, J. F. Mitchell, J. W. Allen, and B. J. Kim, Fermi arcs in a doped pseudospin-1/2 Heisenberg antiferromagnet, Science **345**, 187 (2014).

[31] L. Zhao, D. H. Torchinsky, H. Chu, V. Ivanov, R. Lifshitz, R. Flint, T. Qi, G. Cao, and D. Hsieh, Evidence of an odd-parity hidden order in a spin–orbit coupled correlated iridate, Nat. Phys. **12**, 32 (2016).

[32] J. Jeong, Y. Sidis, A. Louat, V. Brouet, and P. Bourges, Time-reversal symmetry breaking hidden order in $Sr_2(Ir, Rh)O_4$, Nat. Commun. **8,** 15119 (2017).

[33] S. Di Matteo and M. R. Norman, Magnetic ground state of Sr_2IrO_4 and implications for second-harmonic generation, Phys. Rev. B **94,** 075148 (2016).

[34] F. Wang and T. Senthil, Twisted Hubbard Model for Sr_2IrO_4: Magnetism and Possible High Temperature Superconductivity, Phys. Rev. Lett. **106,** 136402 (2011).

[35] Y. K. Kim, N. H. Sung, J. D. Denlinger, and B. J. Kim, Observation of a d-wave gap in electron-doped Sr_2IrO_4, Nat. Phys. **12,** 37 (2016).

[36] Y. J. Yan, M. Q. Ren, H. C. Xu, B. P. Xie, R. Tao, H. Y. Choi, N. Lee, Y. J. Choi, T. Zhang, and D. L. Feng, Electron-Doped Sr_2IrO_4: An Analogue of Hole-Doped Cuprate Superconductors Demonstrated by Scanning Tunneling Microscopy, Phys. Rev. X **5,** 041018 (2015).

[37] R. Comin et al., Symmetry of charge order in cuprates, Nat. Mater. **14,** 796 (2015).

[38] X. Chen, T. Feo, T. A. Harvey, and R. O. Prum, Unidirectional spin density wave state in metallic $(Sr_{1-x}La_x)_2IrO_4$, Nat. Commun. **9,** 103 (2018).

[39] J. Porras, J. Bertinshaw, H. Liu, G. Khaliullin, N. H. Sung et al., Pseudospin-lattice coupling in the spin-orbit Mott insulator Sr_2IrO_4, Phys. Rev. B **99,** 085125 (2019).

[40] H. Liu and G. Khaliullin, Pseudo-Jahn-Teller Effect and Magnetoelastic Coupling in Spin-Orbit Mott Insulators, Phys. Rev. Lett. **122,** 057203 (2019).

[41] J.-H. Chu, J. Hsueh-Hui Kuo, G. Analytis, and I. R. Fisher, Divergent nematic susceptibility in an iron arsenide superconductor, Science **337,** 710 (2012).

[42] S. Kasahara et al., Electronic nematicity above the structural and superconducting transition in $BaFe_2(As_{1-x}P_x)_2$, Nature (London) **486,** 382 (2012).

[43] E. W. Rosenberg, J.-H. Chu, J. P. Ruff, A. T. Hristov, and I. R. Fisher, Divergence of the quadrupole-strain susceptibility of the electronic nematic system $YbRu_2Ge_2$, Proc. Natl. Acad. Sci. U.S.A. **116,** 7232 (2019).

[44] Z. Wang, I. Vinograd, Z. Mei, P. Menegasso, D. Garcia, P. Massat, I. R. Fisher, and N. J. Curro, Anisotropic nematic fluctuations above the ferroquadrupolar transition in $TmVO_4$, Phys. Rev. B **104,** 205137 (2021).

[45] C. W. Hicks et al., Strong increase of T_c of Sr_2RuO_4 under both tensile and compressive strain, Science **344,** 283 (2014).

[46] Z. Guguchia, D. Das, C. N. Wang, T. Adachi, N. Kitajima et al., Using Uniaxial Stress to Probe the Relationship Between Competing Superconducting States in a Cuprate with Spin-Stripe Order, Phys. Rev. Lett. **125,** 097005 (2020).

[47] M. D. Bachmann et al., Spatial control of heavy-fermion superconductivity in $CeIrIn_5$, Science **366,** 221 (2019).

[48] J. G. Vale et al., Importance of XY anisotropy in Sr_2IrO_4 revealed by magnetic critical scattering experiments, Phys. Rev. B **92,** 020406(R) (2015).

[49] F. Ye, S. Chi, B. C. Chakoumakos, J. A. Fernandez-Baca, T. Qi, and G. Cao, Magnetic and crystal structures of Sr_2IrO_4: A neutron diffraction study, Phys. Rev. B **87,** 140406(R) (2013).

[50] L. Hao et al., Giant magnetic response of a two-dimensional antiferromagnet, Nat. Phys. **14,** 806 (2018).

[51] H. Zhang et al., Comprehensive electrical control of metamagnetic transition of a quasi-2D antiferromagnet by in situ anisotropic strain, Adv. Mater. **32,** e2002451 (2020).

[52] J.-W. Kim, S. Chun, Y. Choi, B. Kim, M. Upton, and P. Ryan, Controlling symmetry of spin-orbit entangled pseudospin state through uniaxial strain, Phys. Rev. B **102,** 054420 (2020).

[53] C. Wang, H. Seinige, G. Cao, J. S. Zhou, J. B. Goodenough, and M. Tsoi, Anisotropic Magnetoresistance in Antiferromagnetic Sr_2IrO_4, Phys. Rev. X **4,** 041034 (2014).

[54] I. Fina et al., Anisotropic magnetoresistance in an antiferromagnetic semiconductor, Nat. Commun. **5,** 4671 (2014).

[55] N. Lee, E. Ko, H. Y. Choi, Y. J. Hong, M. Nauman, W. Kang, H. J. Choi, Y. J. Choi, and Y. Jo, Antiferromagnet-based spintronic functionality by controlling isospin domains in a layered perovskite iridate, Adv. Mater. **30,** e1805564 (2018).

[56] H. Wang, C. Lu, J. Chen, Y. Liu, S. L. Yuan, S.-W. Cheong, S. Dong, and J.-M. Liu, Giant anisotropic magnetoresistance and nonvolatile memory in canted antiferromagnet Sr_2IrO_4, Nat. Commun. **10,** 2280 (2019).

[57] See Supplemental Material at http://link.aps.org/supplemental/10.1103/PhysRevLett.129.027203 for experimental details, free energy model and Figs. S1–S9.

[58] M. Ge, T. F. Qi, O. B. Korneta, D. E. DeLong, P. Schlottmann, W. P. Crummett, and G. Cao, Lattice-driven magnetoresistivity and metal-insulator transition in single-layered iridates, Phys. Rev. B **84,** 100402(R) (2011).

[59] C. Hotta, Quantum electric dipoles in spin-liquid dimer Mott insulator κ-$ET_2Cu_2(CN)_3$, Phys. Rev. B **82,** 241104 (R) (2010).